Thermal performance predictions and tests of a novel type of flat plate solar thermal collectors by integrating with a freeze tolerance solution

Article

Accepted Version

It is advisable to refer to the publisher's version if you intend to cite from the work. See Guidance on citing.

To link to this article DOI: http://dx.doi.org/10.1016/j.enconman.2019.111784

Publisher: Elsevier

the End User Agreement.

www.reading.ac.uk/centaur

CentAUR

Central Archive at the University of Reading

Reading's research outputs online

Thermal performance predictions and tests of a novel type of flat plate solar thermal collectors by integrating with a freeze tolerance solution

Jie Deng [a, b], Tadhg S O'Donovan [b], Zhiyong Tian [c,*], Josh King [d], Stuart Speake [e]

[a] School of the Built Environment, University of Reading, Whiteknights, Reading, Berkshire, RG6 6DF, UK

[b] School of Engineering and Physical Sciences, Heriot-Watt University, Edinburgh, Scotland, EH14 4AS, UK

[c] Department of Civil and Environmental Engineering, Norwegian University of Science and Technology, Trondheim, Norway

[d] AES Solar Ltd., Lea Rd, Forres, Scotland, IV36 1AU, UK

[e] Soltropy Ltd., 68 Beechlands Drive, Clarkston, Glasgow, East Renfrewshire, G76 7UX, UK

* Corresponding author:

E-mail address: tianzy0913@163.com; zhiyong.tian@ntnu.no (Z. Tian)

j.deng@reading.ac.uk; deng-jie2@163.com (J. Deng)

Thermal performance predictions and tests of a novel type of flat plate solar thermal collectors by integrating with a freeze tolerance solution

Abstract

A novel design concept of Flat Plate Solar Collectors (FPSCs) is conceived and developed by integrating with a freeze-tolerant (so-called 'ice immune') solution using flexible silicone tubing. It is intended to directly run water in the solar thermal systems with the FPSCs instead of using expensive anti-freeze fluids, and to remove secondary heat transfer facilities (e.g. an extra tank with a buried heat exchanger). Successful development of such kind of solar thermal collectors will enable a reduction of installed cost of conventional solar thermal systems without needing secondary heat transfer facilities. In the prophase design, thermal performances of FPSCs with two configurations, i.e. the serpentine tube type and the header riser type, were predicted based on the collector lumped thermal capacitance model alongside CFD (Computational Fluid Dynamics) calculations. Then two prototypes of FPSCs with the ice-immune silicone tubing (one AES serpentine tube type, one modified Chinese micro-heat-pipe-array panel) were made to determine the collector performance and compared to an original AES solar keymark reference panel via experimental tests. The results show that the Chinese micro-heat-pipe-array panel performs better than the AES header riser solar keymark panel in terms of flow rate per m^2 collector aperture area, while the AES serpentine tube panel with silicone tubing performs somewhat lower than the solar keymark with $T_m^* \leq 0.035$ and better than the solar keymark when

$T_m^* > 0.035$. The serpentine tube panel and the Chinese micro-heat-pipe-array panel both integrated with silicone tubing for freeze tolerance are proven to be effective as the modification doesn't compromise the collector thermal performance markedly.

List of symbols

Nomenclature	
A	area, m^2
A_a	aperture area (or transparent frontal area) of a collector, m^2
A_{inner}	total inner heat transfer areas attached to the aluminum absorber fins, m^2
A_g	gross collector area, m^2
c_p	specified heat capacity, J/(kg K)
D	thickness or diameter, m
F_R	solar collector heat removal factor, $-$
G_g	global solar irradiance on the collector tilted surface, W/m^2
h	heat transfer coefficient, $W/(m^2\,K)$
$h_{e,b-f}$	equivalent convective heat transfer coefficient between the absorber plate and the working fluid, $W/(m^2\,K)$
L	length of collector, m
$\dot{m}_f$	mass flow rate of the collector working fluid, kg/s
N_{serp}	number of the serpentine bend, $-$
Nu	Nusselt number, $-$
Q	heat transfer rate, W
Q_{b-f}	heat transfer rate from the absorbed plate to the flowing water, W
Q_u	useful heat gain of the thermal collector, W
R	equivalent thermal resistance of a heat transfer process, K/W
Ra	Rayleigh number, $-$
S	effective absorbed solar radiation per m^2 by the absorber plate, W/m^2
T	temperature, °C
$T_{ave,b}$	volume-averaged temperature of the whole absorber plate including the copper tubes in CFD calculations, °C
T_f	$= \left(T_{fi} + T_{fo}\right)/2$, characteristic temperature of the working fluid, °C
T_{fi}	collector inlet temperature, °C
T_{fo}	collector outlet temperature, °C
T_m^*	normalized temperature difference in equation (18), $-$
U_{b-f}	equivalent heat transfer coefficient between the absorber plate and the working fluid based on the collector aperture area, $W/(m^2\,K)$
U_{edge}	heat loss coefficient of the collector frame edge, $W/(m^2\,K)$
U_L	collector total heat loss coefficient, $W/(m^2\,K)$
W	width of the collector, m
w	outdoor wind speed, m/s
X_{ij}	shape factor for the radiative heat transfer from surface 'i' to surface 'j', $-$
Greek symbols	

α	absorptance, $-$
β	collector tilted angle, °
ε	emittance, $-$
η_0	$=F_R(\tau\alpha)_{en}$, zero loss collector thermal efficiency in the steady-state model, $-$
η_g	collector thermal efficiency based on the gross area, $-$
θ	incidence angle on the collector tilted surface, °
λ	thermal conductivity, W/(m K)
ρ	reflectance, $-$
σ_b	Stefan-Boltzmann constant, 5.67×10^{-8} W/(m$^2\cdot$K^4)
τ	transmittance of glass cover, $-$
$(\tau\alpha)_{en}$	effective transmittance-absorptance product at normal incidence (or optical efficiency) of the collector, $-$

Subscripts

air	closed air layer between the absorber plate and the glass cover
amb	ambient
b	collector absorber plate
c	convection
cond	conduction
b-f	convective heat transfer between the absorber plate and the working fluid
edge	collector frame edge
edge,air	frame edges of the closed air layer
f	working fluid (water)
fi	collector inlet
fo	collector outlet
g	transparent glass cover
inner	inner surface of the heat transfer tubes of a collector with working fluid
ins	insulation material
*ins*1	bottom surface of the back insulation
r	radiation
r,b-g	radiative heat transfer from the absorber plate to the glass cover
*r,b-ins*1	radiative heat transfer from the absorber plate to the inner surface of the insulation material
r,g- sky	radiative heat transfer from the glass cover to the sky background
*r,ins*1-*amb*	radiative heat transfer from the outer surface of insulation to the ambient
serp	serpentine tube
tube	flowing pipe of the waterway
w	outdoor wind

1 Introduction

Flat Plate Solar Collectors (FPSCs) as a kind of non-concentrating solar thermal collecting device are widely used in low-temperature solar thermal systems, especially for providing domestic hot water [1] and servicing solar district heating plants [2] as well as solar hybrid heat pump systems [3]. It is widely accepted that thermal performance of FPSCs is of paramount concern from the perspective of energy efficiency enhancement [4, 5]. A great deal of work has focused on design, analysis, optimization and improved measures of the collector thermal performance. A common structure of FPSCs consists of a transparent cover, an absorber plate connected to risers and header pipes, back thermal insulation and a metallic frame, as presented in [5]. The common design adopts sheet-and-tube connection between the absorber plate and the header riser pipes [5], such as tube-on-sheet FPSCs [6]. There are different riser configurations for sheet-and-tube flat plate collectors, e.g. brazed bent risers utilized by Gunjo et al. [7], and aluminum corrugated riser tube adopted by Alvarez et al. [8]. Different from the common sheet-and-tube conjunction, Del Col et al. [9] developed a roll-bond absorber plate for FPSCs, and their experimental results showed that the prototype FPSC with a roll-bond absorber could provide higher performance compared to the common sheet-and-tube collectors. In contrast to conventional FPSCs configured with a metallic frame, Chen et al. [10] reported FPSCs fabricated with polymeric materials due to light property of polymers, and found that the efficiency of a polymeric collector was 8−15% lower than that of a traditional metal collector. Nevertheless, they argued that using polymeric materials in the manufacture of solar collectors was

advantageous via a life cycle assessment. Furthermore, there are some other designs of FPSCs, encompassing flow pattern arrangements [11], large size panels [12, 13], novel heat pipe collectors [14], micro-heat-pipe-array collectors [15, 16], minichannel-based collectors [17], evacuated tube type using a hydroformed absorber [18], porous metal foam channel collectors [19, 20], etc. The large size panels are widely used in large solar district heating plants in Denmark [21, 22]. It is noteworthy that the novel micro-heat-pipe-array collectors [15, 16] using aluminum extruded sections can achieve a high zero loss thermal efficiency of 0.80 and is assumed as one of the top level non-concentrating solar collectors among current marketed products.

To improve thermal performance of FPSCs by specific measures, it is intended to attain more absorbed solar radiation on the collector absorber plate and to transfer more thermal energy to the working fluid, meanwhile reducing heat losses from the collector frame composition (i.e. transparent cover at the top, thermal insulation layer at the back as well as frame edges). Optical properties of different selective coatings for the absorber plate are available in [23, 24]. In respect to transferring more thermal energy to the working fluid, using nanofluids as working fluids of FPSCs is proven to be an effective way of heat transfer enhancement, since the nanofluids synthesized by mixing solid, nanometer-sized particles at low concentrations with the base fluid (e.g. water) enable to enhance thermophysical properties of the working fluids in the collectors [25]. It is found that in recent years there are a great number of studies harnessing different types of nanofluids to enhance heat transfer of the working fluids in FPSCs. Sint et al.

[1] declared that using CuO-water nanofluid as the working fluid could improve the collector efficiency by up to 5% compared to that of water under the same conditions via numerical simulation. Moghadam et al. [26] argued that the CuO-water nanofluid with a mass flow rate of 1 kg/min increased the collector efficiency by about 21.8%, and for any particular nanofluid, there is an optimum mass flow rate which maximizes the collector efficiency. Some other types of nanofluids reported in the literature are Cu-Water [27], SiO_2/water [28], MgO/water [29], WO_3/water [30], Al_2O_3/water [31], Al_2O_3/TiO_2–H_2O [32], hybrid of CuO and MgO with MWCNTs/water [33], etc. Verma et al. [34] conducted experimental evaluation on a wide variety of nanofluids for FPSCs and their results showed that the highest rise in energy efficiency of a collector was 23.47%, followed by 16.97%, 12.64%, 8.28%, 5.09% and 4.08%, respectively for graphene/water, CuO /water, Al_2O_3/water, TiO_2/water and SiO_2/water, compared to that of water base fluid type. Although various types of nanofluids have been investigated, the nanofluids with high thermal conductivity and stability are desired for heat transfer enhancement. Sarsam et al. [25] disclosed that carbon-based nanoparticles are the most promising type of nanoparticles that can be dispersed in water at very low concentrations to efficiently enhance the performance of FPSCs. Lower concentration nanofluids will subsequently have higher dispersion stability, lower cost, with minor increases in viscosity, pressure drop, and pumping power. The most significant challenges on using nanofluids in FPSCs can be summarized as the high cost and instability of nanoparticles as well as the increase of viscosity with the resulting increase in frictional pressure drop and pumping power [25].

Additionally, Helvaci and Khan [35] directly took the refrigerant HFC-134a as the working fluid of collectors and stated the collector efficiency rose from 60.2% to 68.8% with a flow rate from 0.001 to 0.01 kg/s. Shojaeizadeh et al. [36] utilized propylene glycol (PG)–water solution (a binary working fluid) for a FPSC and disclosed that increasing PG volume concentration from 25% to 75%, the collector efficiency was increased, while using PG–water at 25%, 100% PG concentrations reduced the collector efficiency to different extents, compared to the case of pure water. Some other measures of heat transfer enhancement for FPSCs can be found in [37, 38] by inserting wire coils or twisted tapes into the collectors.

As a matter of fact, apart from the collector thermal performance issue, freeze tolerance of FPSCs is another pivotal issue impacting maintenance, reliability, durability and cost of relevant solar systems. Since most conventional FPSCs are low-mass modules and have low heat storage capacity, the collector absorber temperature will drop rapidly to freezing point of water at night when outdoor temperature is below 0 °C. Once freezing happens in a collector, the strain caused by the volumetric expansion of water may burst the pipes and cause irreparable damage to the collector [39]. In the cold and severe cold winter regions, it is necessary to adopt special solutions for freeze tolerance in FPSCs and relevant systems. Electric tracing bands employed in solar thermal systems significantly increase the system operating cost and degrade system economy. An effective way of preventing conventional solar thermal systems from freezing when

operating in low-temperature winter environment is utilizing an anti-freeze fluid as the working medium in the systems [40]. However, anti-freeze fluids are usually expensive meanwhile water has to be taken as a secondary heat transfer medium in associated solar thermal systems in view of cheapness and transmission convenience. The secondary heat transfer from the solar thermal system running anti-freeze fluid to the heat storage tank via a heat exchanger will definitely cause investment cost rise of the systems. In this sense, it is not economic to use various complex working fluids (i.e. nanofluids, refrigerants, binary working fluid or antifreeze fluid, etc.) other than water in FPSCs in real engineering, as there is a need to make an independent close-loop, pressurized system for the solar collecting systems, and secondary heat transfer facilities (usually a heat storage tank with a heat exchanger inside) are indispensable in the situation, giving rise to a high installed cost of the solar thermal systems. An open-loop solar heating system with glass heat pipe evacuated tube collectors directly running water [41] can help to save investment cost by circa 30% compared to a close-loop system running anti-freeze fluid at the current China solar market. But there is a potential hazard of freezing in the open-loop solar water system, as the freeze tolerance of the whole system relies upon an electric solenoid valve under the risk of out of operation.

In view of a poor freeze tolerance of conventional FPSCs, the present study aims to develop a novel type of FPSCs by integrating with a special freeze-tolerant solution. As the design concept of the freeze-tolerant solution allows the FPSCs directly running

water without freeze damage (so-called 'ice immune'), it enables an installed cost reduction of relevant solar thermal systems without needing an extra tank for heat exchange and an anti-freeze fluid. Specially, in the UK this will give rise to an installed cost reduction of circa 40% for the conventional solar domestic hot water systems according to a cost estimation. To develop such kind of solar panels, collector thermal performances of two configurations, i.e. the serpentine tube type and the header riser type, were predicted based on the collector lumped thermal capacitance model in the prophase design. Then two prototypes of FPSCs with the ice-immune silicone tubing (one AES [42] serpentine tube panel, one modified Chinese micro-heat-pipe-array panel) were bespoke for determining the collector thermal performance, and were compared with an original AES solar keymark reference panel by experimental tests. It is intended to confirm effective types of freeze-tolerant FPSCs without compromising the collector thermal performance via numerical predictions and experimental tests.

## 2 Design concept of the freeze-tolerant FPSCs

To tolerate ice formation in the tubes of FPSCs, a flexible, compressible silicone tube is inserted into the copper tubes of the collectors to avoid panel damage due to ice expansion under low-temperature conditions below 0 °C. This concept was originally developed by Soltropy Ltd. (Scotland) [43] and used on a heat pipe evacuated tube collector with abreast clamps holding the condenser sections of thermosyphon heat pipes, as illustrated in Figure 1. A compressible silicone tube with 13 mm OD (Outer Diameter)/8 mm ID (Inner Diameter) was inserted into the copper header pipe with 22

mm OD/19 mm ID. Since the inner silicone tubing is compressible, expanded volume

of ice formation will squeeze the wall of silicone tubes for tolerance, thus making the

solar panel an 'ice-immune' system. Collector inlet flow goes through the annular gap

between the outer surface of the silicone tube and the inner surface of the copper tube.

The flow in the annular gap turn arounds at the end of the header pipe and enters into

the inner of the compressible silicone tube till flowing out, meaning that the collector

outlet will return back to the inlet location but from a different flow channel. To separate

the collector inlet and outlet pipes, a T junction is used to assemble the inlet and outlet

pipes, since the silicone tube is flexible and easy to be bent in a vertical branch for the

outflow. Figure 2 provides an image of a prototype header riser FPSC integrated with

silicone tubing. A T junction assembling the collector inlet and outlet is shown in Figure

2(b).

(a)

(b)
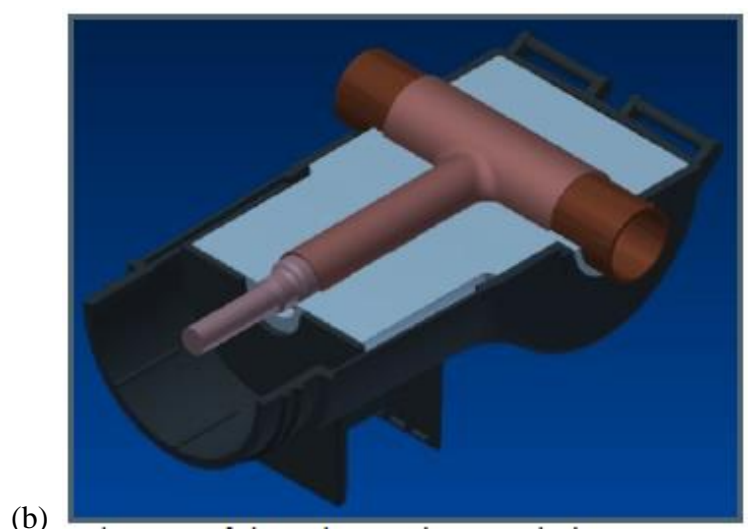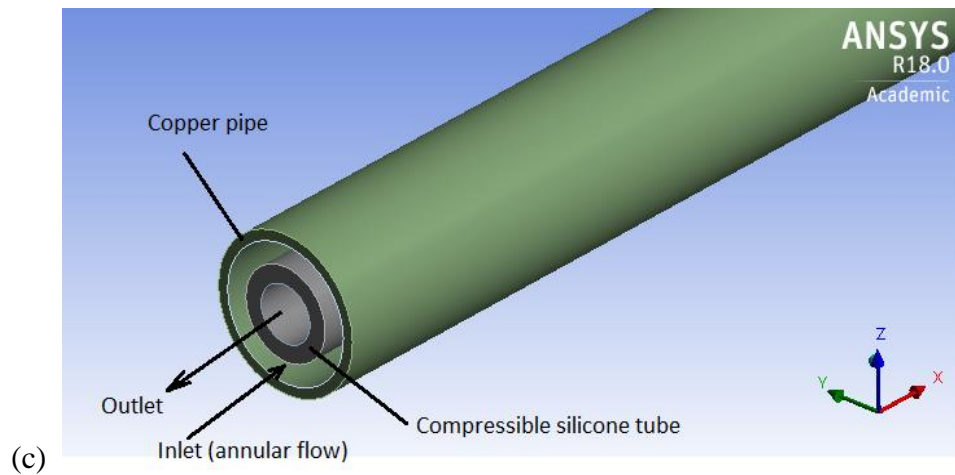
Figure 1 Schematic illustration of the header pipe of a heat pipe evacuated tube collector (a) header pipe; (b) sectional view of a single clamp (c) integration of the header pipe with a compressible silicone tube
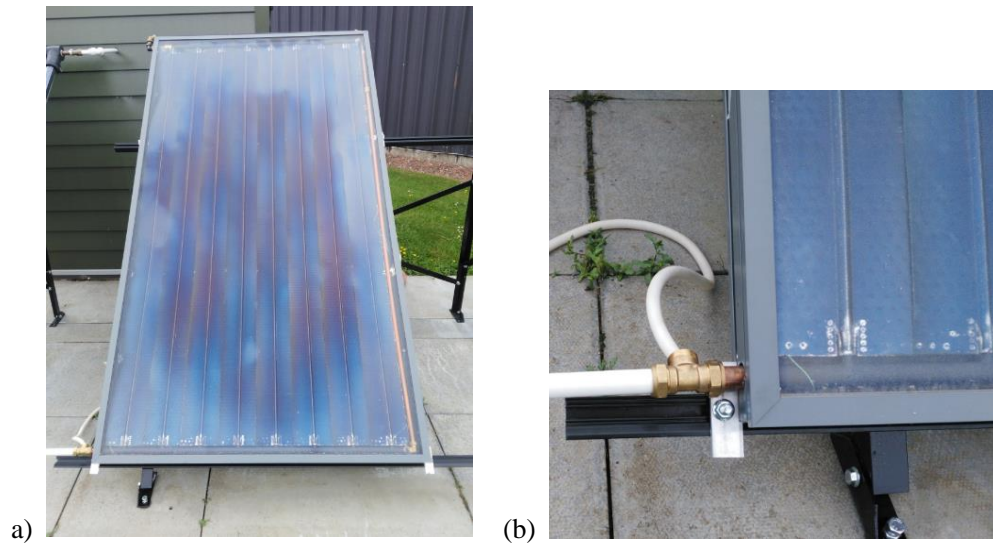
Figure 2 Image of the header riser FPSC (a) full size; (b) enlarged view of the lower left corner with a *T* junction assembly for collector inlet and outlet

In the preliminary design, two configurations of FPSCs, i.e. the serpentine tube and the header risers, were considered for a comparison. For the serpentine tube type, the

compressible silicone tube is inserted along the serpentine tube shown in Figure 3(a), while for the header riser type sketched in Figure 3(b), only the header pipe and side pipe is integrated with the compressible silicone tube, as the riser pipe diameter (e.g. 10 mm OD) is usually smaller than the silicone tube. Ice formation would probably occur first in the riser pipes due to a smaller diameter and faster heat loss, but ice formation process within the pipes is not an instantaneous process. Once ice is generated from the riser pipe walls, expansion of the ice produces a positive pressure pushing water to the header pipes where the wall of silicone tubes can tolerate volume expansion. Thus, it is assumed that the expansion of ice formation in the riser tubes can stretch to the header pipe for freeze tolerance.
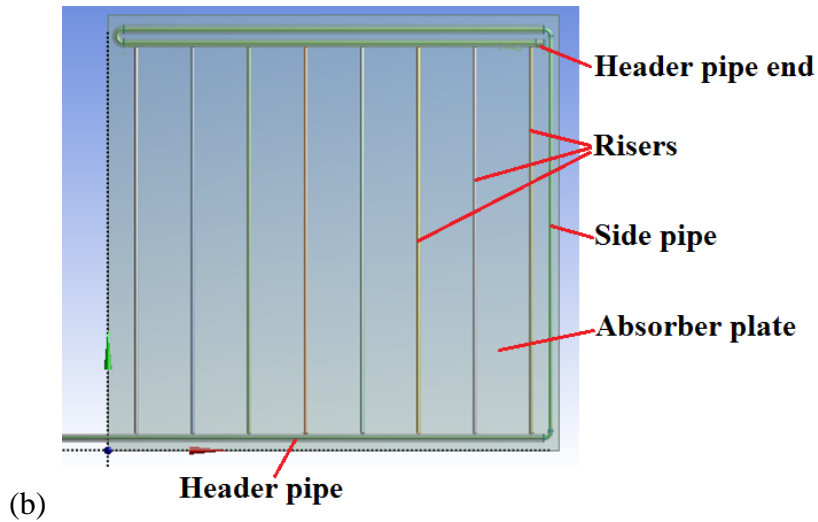

Serpentine tube

Absorber plate

(a)

(b)
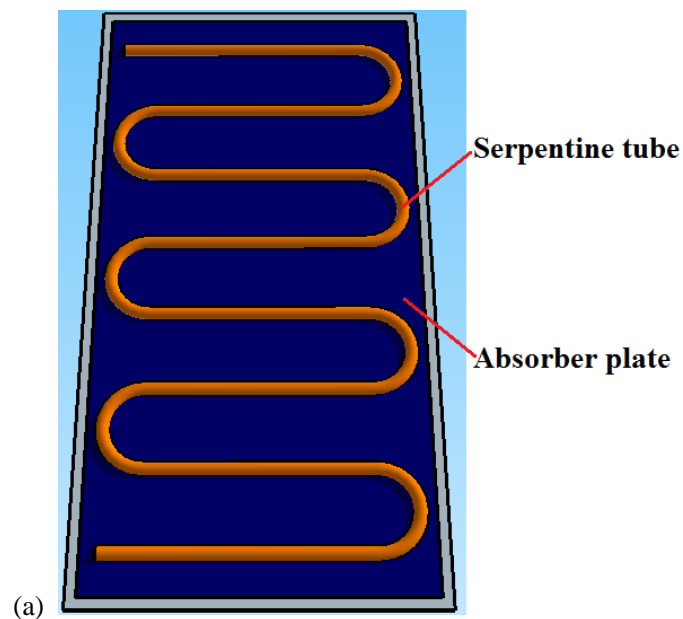
Figure 3 Sketch of two configurations of FPSCs (a) serpentine tube; (b) header riser

3 Methods and conditions

3.1 Numerical prediction model of the collector thermal performance

Numerical prediction is an economic way of guiding preliminary design of the FPSCs, thus it is conducted to inform the design process of prototype modules for further tests. Due to complexity of coupled heat transfer processes involving conduction, convection and radiation within the FPSCs, the collector thermal performance model will be primarily established based on the lumped thermal capacitance parameter method. The numerical model will be validated with the test result of a bespoke prototype collector.

3.1.1 Lumped thermal capacitance parameter model of FPSCs

Figure 4 delineates the thermal resistance network diagram of commonly single glass cover FPSCs based on the lumped thermal capacitance parameter method. A set of thermal balance equations of the collector components (g – glass cover, air – closed air

layer, *b*- absorber plate, *f* – working fluid and *ins1* – insulation bottom surface) is established to describe the collector thermal performance in the steady-state, neglecting the thermal capacitances of the collector components. General assumptions of the collector model are referred to [23].
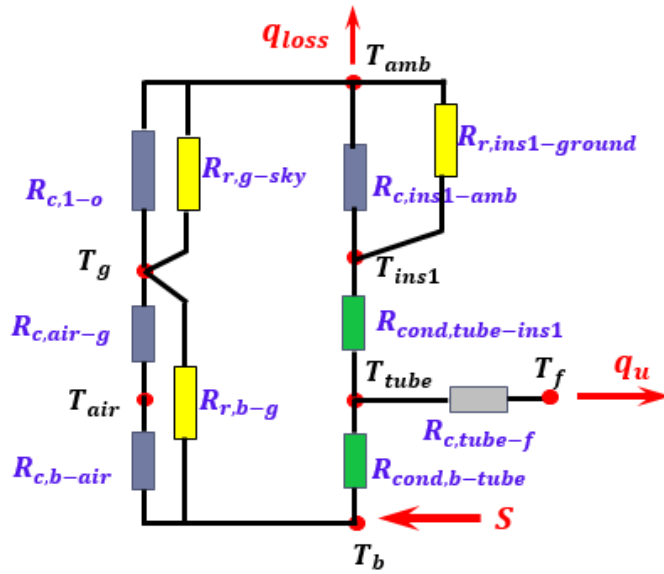

Figure 4 Thermal resistance network of the heat transfer process in a single glass cover flat plate collector *b* – absorber plate; *f* – working fluid; *air* – closed air layer; *g* – glass cover; *ins*1 – insulation bottom; *amb* – ambient; *R* – thermal resistance; *c* – convection; *cond* – conduction; *r* – radiation

For the top glass cover – *g*:

$$\alpha_g G_g + (h_w + h_{r,g-sky})(T_{amb} - T_g) + h_{c,air-g}(T_{air} - T_g) + h_{r,b-g}(T_b - T_g) = 0$$

(1)

For the closed air layer between the absorber plate and the glass cover – *air*:

$$h_{c,b-air}(T_b - T_{air}) + h_{c,g-air}(T_g - T_{air}) + U_{edge,air-amb}\frac{A_{edge,air}}{A_a}(T_{amb} -$$

16

$$T_{air}) = 0 \tag{2}$$

For the absorber plate – b:

$$(\tau\alpha)_{en}G_gA_a - h_{c,b-air}A_a(T_b - T_{air}) - h_{r,b-g}A_a(T_b - T_g) + \lambda_{ins}\frac{A_{ins1}}{D_{ins}}(T_b -$$

$$T_{ins1}) - h_{e,b-f} \cdot A_{inner}(T_b - T_f) = 0 \tag{3}$$

where the effective transmittance-absorptance $(\tau\alpha)_{en}$ is calculated by [23]:

$$(\tau\alpha)_{en} = \tau_g\alpha_b \sum_0^\infty[(1 - \alpha_b) \cdot \rho_g]^n = \frac{\tau_g\alpha_b}{1-(1-\alpha_b)\rho_g} \tag{4}$$

For the working fluid (water) – f:

$$h_{e,b-f} \cdot A_{inner}(T_b - T_f) - \dot{m}_f c_{p,f}(T_{fo} - T_{fi}) = 0 \tag{5}$$

where the characteristic temperature of water can be considered as the arithmetic mean

temperature $T_f = (T_{fi} + T_{fo})/2$, meaning that $T_{fo} = 2T_f - T_{fi}$ can be used to

reduce the unknown variable T_{fo}.

For the insulation bottom surface – $ins1$:

$$\lambda_{ins}\frac{A_{ins1}}{D_{ins}}(T_b - T_{ins1}) - (h_w + h_{r,ins1-ground})(T_{ins1} - T_{amb}) = 0 \tag{6}$$

3.1.2 Calculations of heat transfer coefficients

The radiative heat transfer coefficient between the glass cover and sky background is

calculated by equation (7) and the sky background temperature T_{sky} is given by [44].

The convective heat transfer coefficient between the glass cover surface and ambient is

calculated by equation (8) [45].

$$h_{r,g-sky} = \frac{\varepsilon_g\sigma_b}{T_{amb}-T_g}(T_g^4 - T_{sky}^4), \ T_{sky} = 0.0552T_{amb}^{1.5} \tag{7}$$

$$h_w = 6.5 + 3.3w \quad (w < 6 \text{ m/s}) \tag{8}$$

The natural convective heat transfer in the closed air layer between the top glass cover and the absorber plate is determined by Holland's correlation [23, 46]:

$$Nu = 1 + 1.44\left\{1 - \frac{1708(\sin 1.8\beta)^{1.6}}{Ra\cos\beta}\right\}\left[1 - \frac{1708}{Ra\cos\beta}\right]^+ + \left[\left(\frac{Ra\cos\beta}{5830}\right)^{1/3} - 1\right]^+ \quad (9)$$

where the Rayleigh number $0 < Ra < 10^5$ and collector tilted angle $0 \leq \beta < 60°$.

The radiative heat transfer coefficients between surfaces 'i' and 'j', such as $h_{r,b-g}$, and $h_{r,g-sky}$, are calculated by equation (10).

$$h_{r,i-j} = \frac{\sigma_b(T_i + T_j)(T_i^2 + T_j^2)}{(1-\varepsilon_i)/\varepsilon_i A_i + 1/X_{ij}A_i + (1-\varepsilon_j)/\varepsilon_j A_j} \quad (10)$$

Additionally, the heat loss coefficient from the collector frame edges to the ambient is defined as:

$$U_{edge,air-amb} = \left(\frac{1}{h_w} + \frac{D_{edge}}{\lambda_{ins}}\right)^{-1} \quad (11)$$

3.1.3 Equivalent heat transfer coefficients of the absorber plates determined by CFD calculations

The flow and heat transfer of the serpentine tube and the header risers with freeze-tolerant silicone tubes are complicated 3-D problems. For the serpentine tube, there is a number of bends and elbows (7 bends in Figure 3(a)) and the whole tube is encompassed by a thin aluminum absorber fin (0.5mm thickness). As for the header risers, a number of parallel-flow riser tubes (8 riser tubes in Figure 3(b)) attached to the absorber fin are connected to the header pipe integrated with the silicone tubing, which makes the flow different from a one-dimensional circular tube flow. The flow is a combination of annular gap flow and internal flow within the silicone tubes. There is

no empirical correlation of heat transfer coefficients (or Nusselt number) available for the complicated geometry structure of the serpentine tube and the header risers integrated with silicone tubes.

To get the equivalent conduction-convection heat transfer coefficient ($h_{e,b-f}$) from the absorber plate to the working fluid for numerical predictions, the commercial CFD (Computational Fluid Dynamics) software package ANSYS FLUENT 18.0 [47] has been employed to establish the physical models and to solve the fluid-solid conjugate heat transfer of the absorber plate, the copper tubes and the working fluid (water). The calculated equivalent heat transfer coefficients of the absorber plates are then embedded into the lumped capacitance model to perform the collector performance predictions. The coupled heat transfer from the absorber plate to the flowing water is assumed as a steady-state problem and the laminar flow regime is considered here, since it is found that the Reynolds number for the internal flows is lower than 4000 (there is a small deviation when using a transitional flow model for Reynolds number between 2300 and 4000). The governing equations describing the flow and heat transfer of the absorber plates with different configurations consist of continuity, momentum and energy equations in terms of the Navier – Stokes equations [48], as given by Equations (12)–(14) in Cartesian coordinates.

The continuity equation:

$$\nabla \cdot u = 0 \tag{12}$$

The momentum equation:

$$(\rho u \cdot \nabla)u = -\nabla p + \nabla \cdot \tau \qquad (13)$$

The energy equation:

$$\rho c_p u \cdot \nabla T = \nabla \cdot (k\nabla T) \qquad (14)$$

where u is the velocity vector; p is the pressure vector; τ is the tension vector.

The gross area of the FPSC in simulation is 2150 mm×1150 mm (L×W). The selected specification and design conditions for the collector performance predictions are shown in Table 1. To reduce the computational effort, the computation domains for the absorber plates were tailored, which would not affect the calculation results since the heat transfer coefficient is an inherent characteristic of specific surface structures. Figure 5(a) shows the geometric model of the serpentine tube absorber plate in a reduced computational domain of half length, which comprises the aluminium absorber plate (thickness 0.5mm), the entry pipe (150 mm extend length out of the absorber plate) and the serpentine tube with 3 bends (half circle, diameter 130 mm). An enlarged view of the entry pipe of the serpentine tube is illustrated in Figure 1(c). A hybrid mesh of 870,002 cells consisting of hexahedron cells and wedge cells was generated with the cell size over the range of 0.5mm to 4mm, as a grid independence test showed that the calculated equivalent heat transfer coefficients of the intermediate mesh with 870,002 cells was nearly the same as that of a fine mesh with 1,017,541 cells for the computational domain of the serpentine tube absorber plate. Figure 5(b) gives the reduced computation domain of a quarter of the header riser absorber plate. Structure of the entry pipe of the header pipe is similar to that of the serpentine tube. A hybrid

mesh of 1,142,136 cells comprising tetrahedron cells, wedge cells, hexahedron cells

and pyramid cells was chosen for the header risers by a grid independence examination.

Table 1. Specified conditions and parameters of the flat plate solar collector

| Dimensions	$2150 \times 1150 \times 65$ (mm)
	Frame width $D_{edge} = 25$ mm
Transparent cover	Tempered glass with 3.2 mm thickness
	Transmittance $\tau_g = 0.92$
	Emittance $\varepsilon_g = 0.07$
	Spacing between the glass cover and the absorber plate: 25 mm
Absorber	Aluminium fin
	Selective coating surface $A_a = 2.31$ m^2
	Absorptance $\alpha_b = 0.92$
	Emittance $\varepsilon_b = 0.15$
	Thermal conductivity $\lambda_b = 170$ W/(m K)
Tubes for serpentine tube configuration	Annular duct with external copper pipe (OD/ID: 22/19 mm) inserted by silicone tubing (OD/ID: 13/8 mm);
	Number of bends: 7
	Thermal conductivity of cooper: 380 W/(m K)
	Thermal conductivity of silicone tubing: 0.0695 W/(m K)
Tubes for header riser configuration	Annular duct for the headers at the bottom and top as well as on the right side of the riser pipes, the size of which is identical to that of the serpentine tube;
	rhombic copper tube waterway for the riser tubes without inner tubing, outer diameter 10 mm and 0.5 mm thickness;
	Number of riser tubes: 8
Working fluid	Water
	$c_p = 4187$ (J/kg K)
Thermal insulation	PIR (polyisocyanurate) board at bottom and frame edges
	Thermal conductivity $\lambda_{ins} = 0.021$ W/(m K)
	Thickness at bottom: 25–100 mm
	Thickness at the frame edges: 25 mm

(a)

(b)
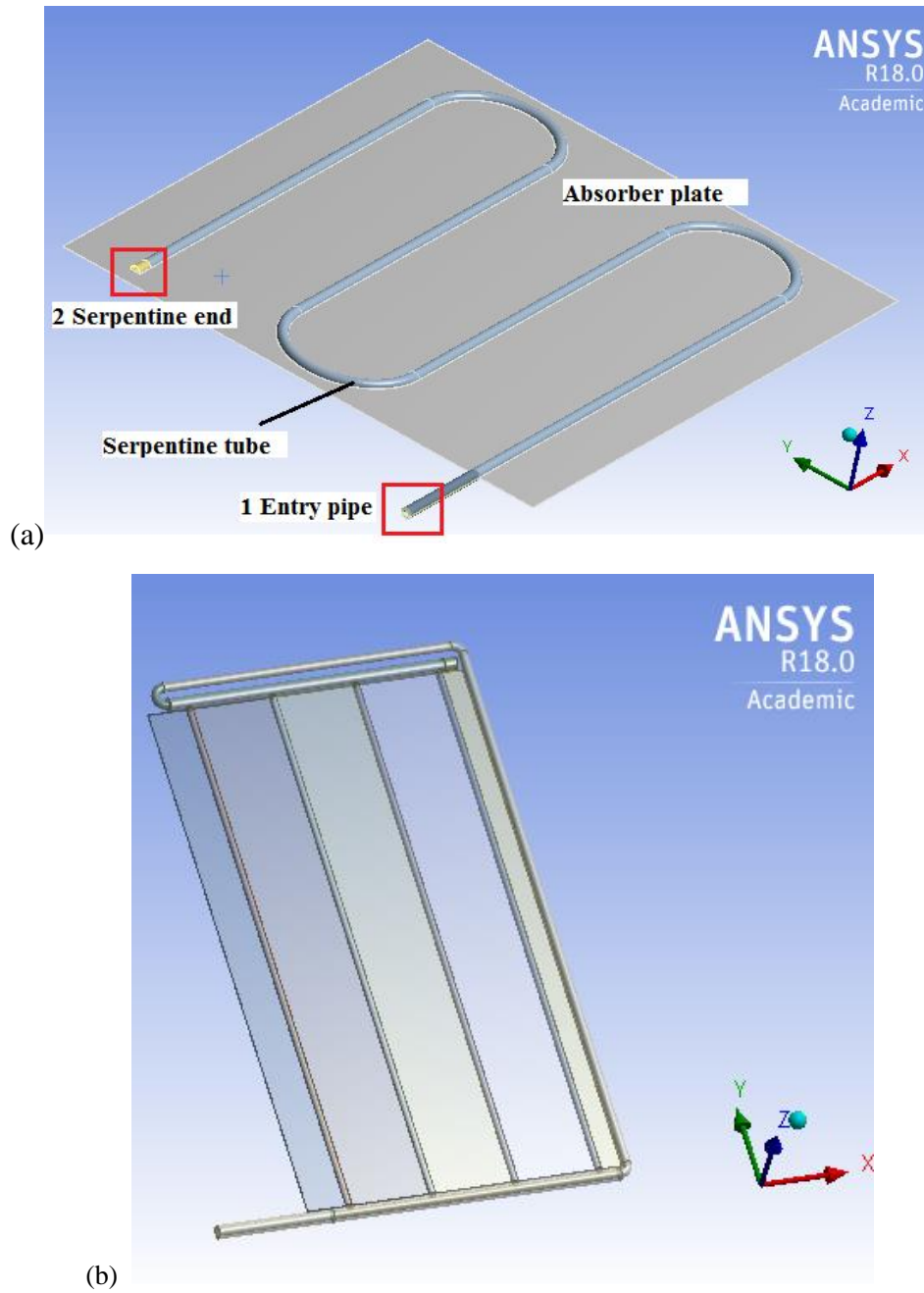
Figure 5 Reduced computational domain of (a) the serpentine tube absorber plate (half

the length of the whole absorber plate); (b) a quarter of the header riser absorber plate

Regarding the CFD calculation conditions, an inlet velocity of 0.2653 m/s was set for

the annular cross-section of the entry pipe between the outer copper tube and the inner

silicone tube, corresponding to a volumetric flow rate of 2.4 l/min. Calculations of

water properties (density, dynamic viscosity, thermal conductivity and specific heat capacity) were referred to Fan and Furbo [49]. Four inlet temperature conditions, 10 °C, 30 °C, 50°C, 70 °C, were considered. The outlet of the silicone tube within the entry pipe was set as 'outflow' condition. It was presumed that the equivalent conduction-convection heat transfer coefficient is independent of the absorber plate heat loss to the air above it, because the corresponding thermal resistance comprising the thermal conduction resistance from the absorber plate to the serpentine tube/riser pipes and the convective heat transfer thermal resistance from the copper tubes to the flowing water could be assumed as a constant in specific conditions. In this sense, the top surface of the absorber plate was set as fixed heat flux boundary condition regardless of heat loss to the air above. A heat flux of 676 W/m^2 was set on the top surface of the absorber plate as well as the top half surfaces of the copper tubes, considering 800 W/m^2 solar irradiance and an effective transmittance-absorptance product of 0.845 for the absorber plate. The back of the absorber plate towards the thermal insulation layer was set as an adiabatic wall. Flow-solid and solid–solid contact surfaces were set as coupling wall boundaries. As to the solution, the pressure-based solver [47] was used to solve the equations based on the finite volume method. The second-order upwind scheme was chosen as the differencing scheme of the convective terms of the momentum equations. The SIMPLEC algorithm [47] was adopted to deal with the coupling of the pressure and velocity. The solution convergence was judged by the control accuracies of residuals of the continuity and momentum equations to be less than 10^{-3} meanwhile that of the energy equations to be less than 10^{-6}, or the residuals of the calculated case

tend to be flat and the characteristic parameters (e.g. the outlet temperature and the equivalent heat transfer coefficient) tend to be constant.

The equivalent conduction-convection heat transfer coefficient from the absorber plate to the flowing water was then calculated by equation (15) based on the CFD results.

$$h_{e,b-f} = \frac{Q_{b-f}}{A_{inner}[T_{ave,b} - (T_{fi} + T_{fo})/2]}$$ (15)

Please find the symbols in the nomenclature. Specially, for the serpentine tube, A_{inner} is chosen as the internal surface area of the outer copper tube with meander lines, while for the header risers, it is considered as the internal surface area of all the riser tubes.

3.1.4 Solving method of the collector lumped capacitance model

A set of equations describing the thermal balance of the collector components (equations (1)–(6)) is rearranged as a matrix equation of $AT = b$, which is usually solved iteratively [50], e.g. Gauss-Seidel iteration. Initial temperature values of the collector components should be assigned to calculate the initial heat transfer coefficients for proceeding the iteration. The convergence criteria is judged by the control accuracy of the norm of temperature vector ($T = [T_g, T_{air}, T_b, T_f, T_{ins1}]^{'}$) difference between the former ((i-1)th) and the present (i^{th}) iterative steps, as given by equation (16):

$$\|x^{i-1} - x^i\| \leq 10^{-8}$$ (16)

3.1.5 Parameter definition

In the predictions, the collector tilted angle was chosen as $\beta = 45°$ (the same as the

installed panels in test) and global solar irradiance on the tilted surface was set as $G_g=$ 800 W/m^2. Outdoor wind speed was set to be $w = 3$ m/s and ambient temperature was 10 °C. The collector thermal efficiency (η_g) based on the gross collector area (A_g) was then calculated based on the collector lumped capacitance model in section 3.1.1 by specifying the collector inlet temperatures (T_{fi}). The collector thermal efficiency (η_g) based on A_g is defined in equation (17) [51]. To get the collector thermal efficiency curve ($\eta_g - T_m^*$), different inlet temperatures (10 °C, 30 °C, 50°C, 70 °C) were selected to obtain various normalized temperature differences (T_m^*) by equation (18) [51].

$$\eta_g = \frac{Q_u}{A_g G_g} = \frac{\dot{m}_f c_{p,f}(T_{fo}-T_{fi})}{A_g G_g} \tag{17}$$

$$T_m^* = \frac{T_{fi}-T_{amb}}{G_g} \tag{18}$$

The collector thermal efficiency (η_a) based on collector aperture area (A_a) is defined as:

$$\eta_a = \frac{Q_u}{A_a G_g} = \frac{A_g}{A_a}\eta_g \tag{19}$$

Concerning the collector thermal efficiency curve correlating η_g (or η_a) with T_m^*, a simple linear model in equation (20) is commonly used to describe the collector steady-state thermal performance [23].

$$\eta_g = \frac{A_a}{A_g} \cdot \left[F_R(\tau\alpha)_{en} \cdot K_{\theta b}(\theta) - F_R U_L \frac{(T_{fi}-T_{amb})}{G_g} \right] \tag{20}$$

where the incidence angle modifier $K_{\theta b}(\theta)$ of solar beam radiation is described as [23]:

$$K_{\theta b}(\theta) = 1 - b_0 \cdot \left(\frac{1}{cos\,\theta} - 1 \right) \tag{21}$$

where b_0 is a dimensionless coefficient of the incidence angle modifier for a FPSC.

3.2 Experimental tests for determining thermal performance of FPSCs

Thermal performance tests of three FPSCs have been carried out at HWU (Heriot-Watt University) Dubai campus. The panels included an original header riser panel without freeze-tolerant tube (panel 1–AES reference panel with a solar keymark certificate), a bespoke serpentine tube panel integrated with flexible silicone tubing (panel 2), and a Chinese micro-heat-pipe-array panel modified with flexible silicone tubing (panel 3). Figure 6 shows an image illustration of the three panels in test. All the three panels were connected in series with a tilted angle of 45° and their thermal performances were tested simultaneously. Brief descriptions of the solar panels are as follows:

- Panel 1: an original AES header riser panel with a collector gross area of 1.5 m^2 (1.3 m×1.15 m; aperture area 1.38m^2) without freeze-tolerant tube; 25 mm thickness PIR board insulation.

- Panel 2: an AES prototype 22 mm copper serpentine tube panel with 14 mm OD/8mm ID flexible silicone tube and with a gross area of 1.5 m^2 (1.3 m×1.15 m; aperture area 1.38 m^2); 25 mm thickness PIR board insulation.

- Panel 3: a Chinese micro-heat-pipe-array panel with a gross collector area of 2 m^2 (2 m×1 m×0.09 m; aperture area of 1.853 m^2) and the header pipe of 20 mm diameter was inserted with a flexible silicone tube of 15mm OD/8 mm ID; 50 mm rock wool thermal insulation board at the back.
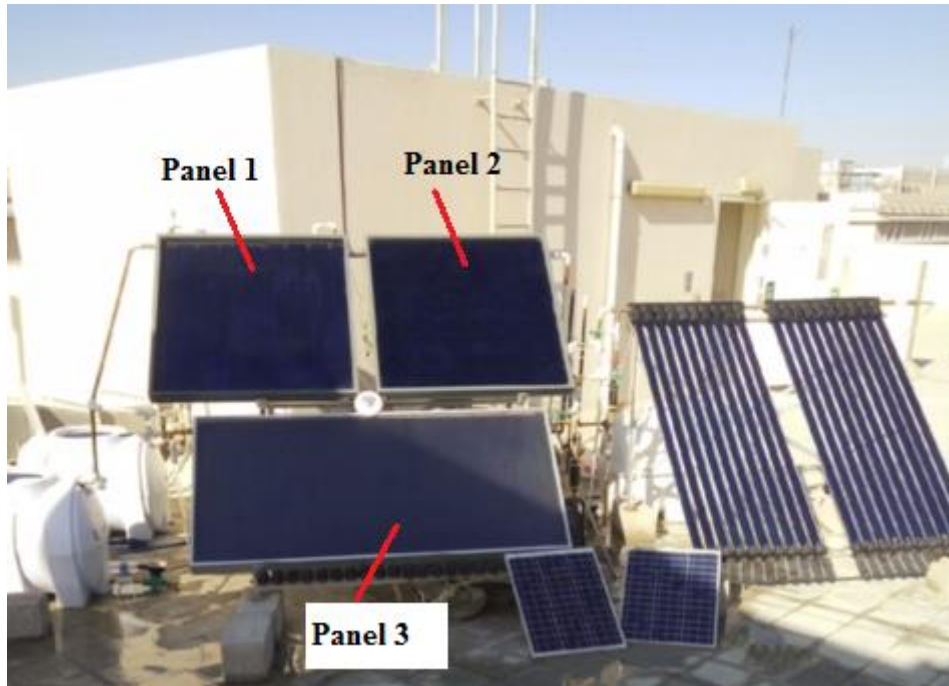
Figure 6 Image of three solar thermal collectors tested on HWU Dubai campus

A collector thermal efficiency curve of the original AES Ltd. header riser panel (panel 1) without freeze-tolerant tube is available from the solar keymark certificate issued by DIN CERTCO, Germany in 2014, as given by equation (22) with a flow rate of 1.74 l/min. The panel 1 was taken as a reference benchmark of the test accuracy, allowing comparison of different collector thermal performances. According to the collector thermal performance test standard [51], collector inlet and outlet temperatures, ambient temperature, global solar irradiance incident on the collector tilted surface and volumetric flow rate through the collectors, were recorded via a data acquisition system written in LabView programming. All the test instruments were calibrated before the test executions. Volumetric flow rates over the range of 1.6–2.3 l/min were considered to make a comparison of collector performance disparity under various flow rate conditions. Experimental test data was then analyzed to determine the thermal

performances of the specific solar thermal collectors in terms of collector thermal efficiencies.

$$\eta_g = A_a/A_g(0.788 - 5.028\, T_m^* - 0.009 G_g T_m^{*2}) = 0.725 - 4.626\, T_m^* - 0.008 G_g T_m^{*2} \quad (22)$$

Due to a limitation of the test rig, the collector inlet temperature couldn't be adjusted to be constant under a certain test condition following the test standard [51]. In this situation, a small variation of the collector inlet temperature (typically $\pm 1\ °C$) in a small time interval of 3–5 min was assumed as the steady-state condition for obtaining effective testing points. Meanwhile, the effective testing points should meet the requirements of relatively stable solar irradiance in the time interval within a variation range of $\pm 50\ W/m^2$ [51]. Furthermore, a wide range of collector inlet temperature was implemented via reducing water volume of the tanks connected to the collectors in the loop to attain different reduced temperature difference conditions under a flow rate of 1.7 l/min, in order for determining the collector thermal performance. Test results were compared to the AES header riser reference panel from the solar keymark certificate. Additionally, for the case of flow rate at 2.3 l/min, the collector thermal efficiencies close to the zero loss thermal efficiency were performed.

4 Results and discussion

4.1 Prophase design based on collector thermal performance predictions

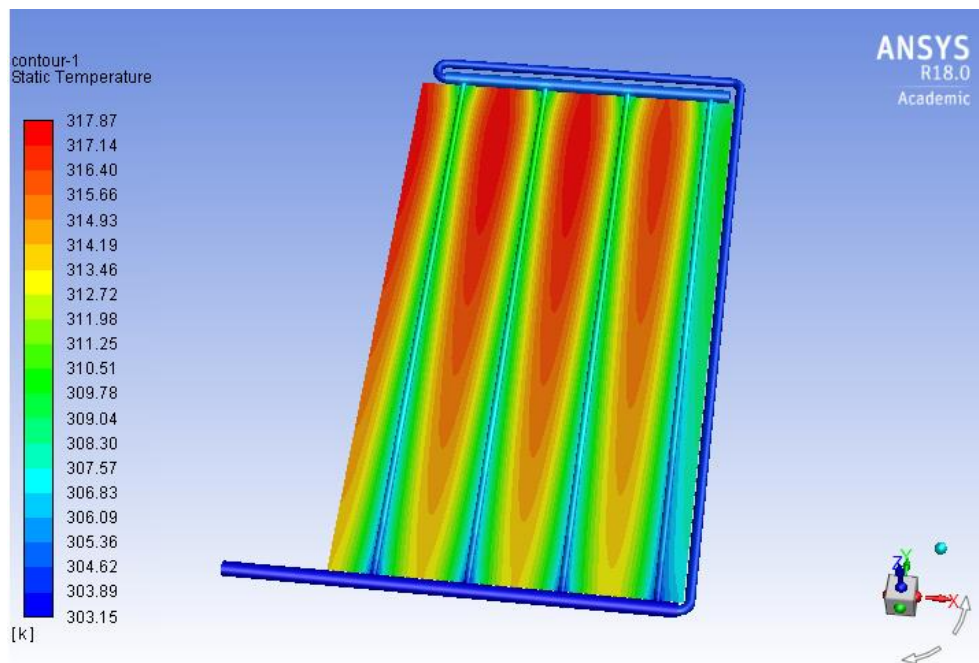**4.1.1 Equivalent heat transfer coefficient of the absorber plates**

Four inlet temperature conditions, 10 °C, 30 °C, 50 °C, 70 °C, were considered to obtain equivalent heat transfer coefficients of the absorber plates ($h_{e,b-f}$) for the collector thermal performance predictions. Two configurations of solar collectors, i.e. the serpentine tube and the header riser types were concerned. CFD calculations showed that for a specific configuration, temperature contours of absorber plates with different inlet temperatures were similar to each other except the temperature scale. For the serpentine tube absorber plate, the absorber temperature contour with an inlet temperature of 30 °C is shown in Figure 7(a). It suggests that the temperature near the serpentine tube is much lower than the middle space between adjacent parallel parts of the tube. The temperature gradient is mainly due to fin efficiency of the absorber plate. For the header riser type, the absorber plate temperature contours at four different inlet temperatures are analogous to each other as well except the temperature scale. Figure 7(b) gives the temperature contour of the header riser absorber plate with 30 °C inlet temperature. In contrary to the temperature contour of the serpentine tube type, it is found that the maximum temperature of the header riser absorber plate in an identical inlet temperature condition is much lower than that of the former.

The equivalent conduction-convection heat transfer coefficients at different inlet temperatures were obtained by equation (15), using the temperature field information from the CFD calculations. Table 2 lists the calculated results for the serpentine tube and the header riser absorber plates. The values of equivalent heat transfer coefficients of the header risers are much higher than those of the serpentine tube, mainly because

the inner heat transfer area (A_{inner}) of the two absorber plates were chosen differently,

as declared in section 3.1.3.
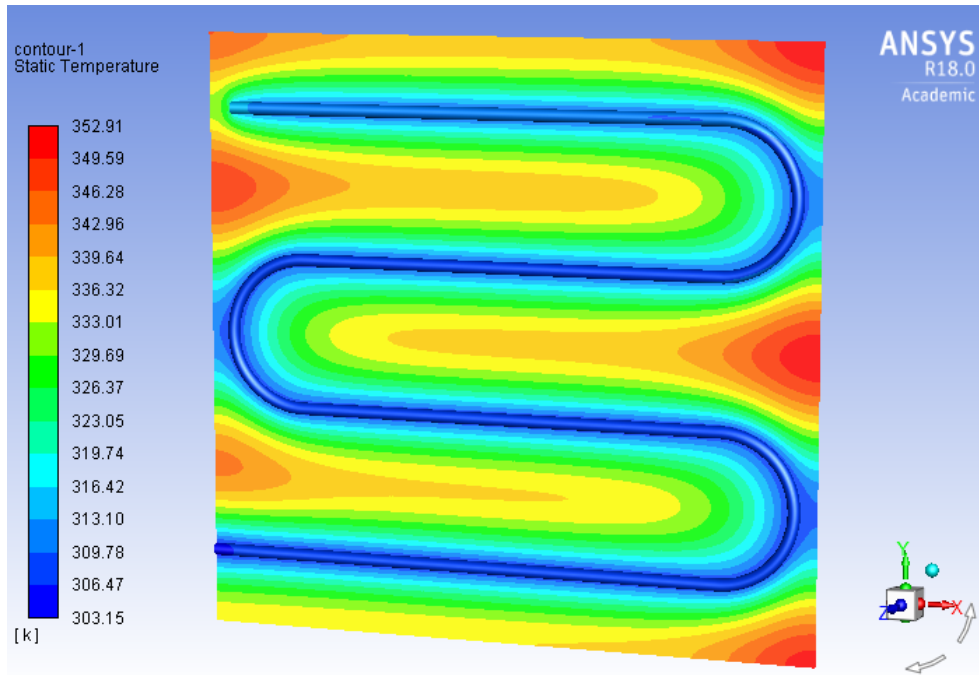
(a)

(b)

Figure 7 Temperature contours of absorber plates at 30 °C inlet temperature (a) the

serpentine tube; (b) the header risers

Table 2. Calculated equivalent heat transfer coefficients of the absorber plates

T_{fi}	$h_{e,b-f}$ (W/(m^2 K))	
	The serpentine tube	The header risers
10 °C	165.0	422.7
30 °C	167.3	437.6
50 °C	171.4	453.4
70 °C	176.6	467.7

Note: For the serpentine tube, A_{inner} was chosen as the internal surface area of the outer copper tube with meander lines, while for the header risers, it's chosen as the internal surface area of all the riser tubes.

4.1.2 Model validation based on a bespoke AES serpentine tube panel

Based on the numerical prediction model of the collector thermal performance established in section 3.1, Matlab programs of the steady-state collector performance with two different configurations were written to calculate the collector performance. The equivalent heat transfer coefficients of the absorber plates obtained by CFD analysis in section 4.1.1 were embedded in the model calculations. Before going to predict the collector performance, it is necessary to validate the collector thermal performance model. A bespoke prototype AES serpentine tube solar panel with a gross area of 1.5 m^2 and an aperture area of 1.38 m^2 integrated with 14 mm OD/8mm ID flexible silicone tubing (the panel 2 stated in section 3.2) was adopted for the model validation. The bent number of the serpentine tube was four for the solar panel 2. The volume flow rate in the experiment was 1.7 l/min. The same condition as the experiment was considered for the model validation. Some other parameters of the solar panel can be found in Table 1. Figure 8 gives a comparison of the numerical result compared to the experimental data in relation to the panel 2. The calculated zero loss collector

thermal efficiency and total heat loss coefficient for the panel 2 are 71.0% and 3.553 W/(m² K), respectively, while corresponding values by experiment are 63.1%, 2.896 W/(m² K), respectively. It indicates that the numerical calculation overestimates the zero loss collector efficiency by 12.5% and the total heat loss coefficient by 22.7%. The deviation is mainly due to the adoption of the lumped thermal capacitance model and model assumptions as well as the measuring uncertainties of the tests. The experimental data will be explained in the next section.

$\eta_{g\_numerical} = 0.710 - 3.553\, T_m\,^*$
$R^2 = 0.999$

$\eta_{g\_experiment} = 0.631 - 2.896\, T_m\,^*$
$R^2 = 0.754$

▲ Measured data points
○ Numerical calculation
── Linear fitting_experiment
— — Linear fitting_numerical calculation

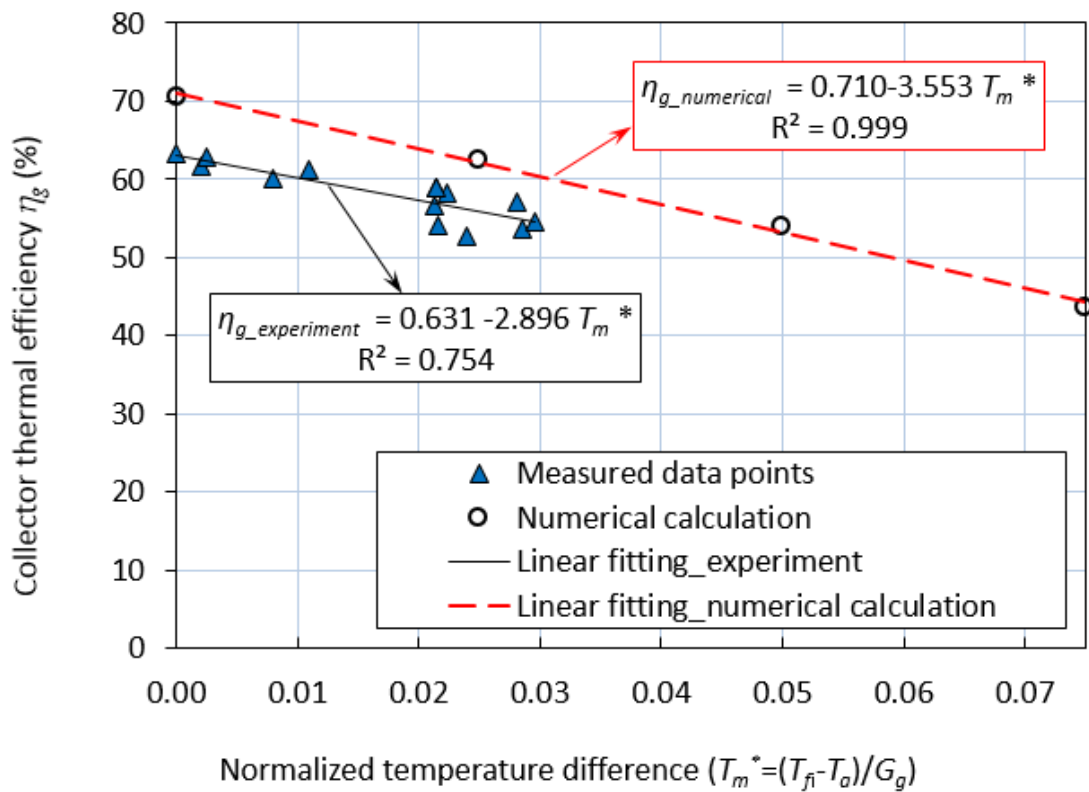Normalized temperature difference ($T_m\,^* = (T_{fi} - T_a)/G_g$)

Figure 8 Numerical calculation of the serpentine tube panel integrated with silicone tubing (solar panel 2 in section 3.2) compared to the experimental data

4.1.3 Collector thermal performance predictions

To compare the difference of two configurations, i.e. the serpentine tube and the header

risers, numerical predictions with both configurations were implemented by incorporating the equivalent heat transfer coefficients of the absorber plates obtained by the CFD calculations. The collector parameters were chosen as listed in Table 1. A volume flow rate of 2.4 l/min (0.017 kg/(s) per m^2 collector aperture area) was considered in the calculations. Figure 9 shows the prediction results of the two configurations with different thermal insulation thicknesses. The collector thermal performance parameters of different cases are listed in Table 3. In an identical condition of thermal insulation thickness, the zero loss collector thermal efficiencies (η_0) of the serpentine tube are 3.4–3.9% lower than that of the header riser, while the collector total heat loss coefficients (U_L) of the serpentine tube are nearly the same as that of the header risers. It indicates that the header riser flat plate collector integrated with silicone tubing performs slightly better than the serpentine tube type. Furthermore, a comparison of different insulation thicknesses with the same configuration suggests that increasing the thermal insulation thickness of PIR board above 50 mm has a minor impact on the collector thermal performance improvement for the studied solar collectors.
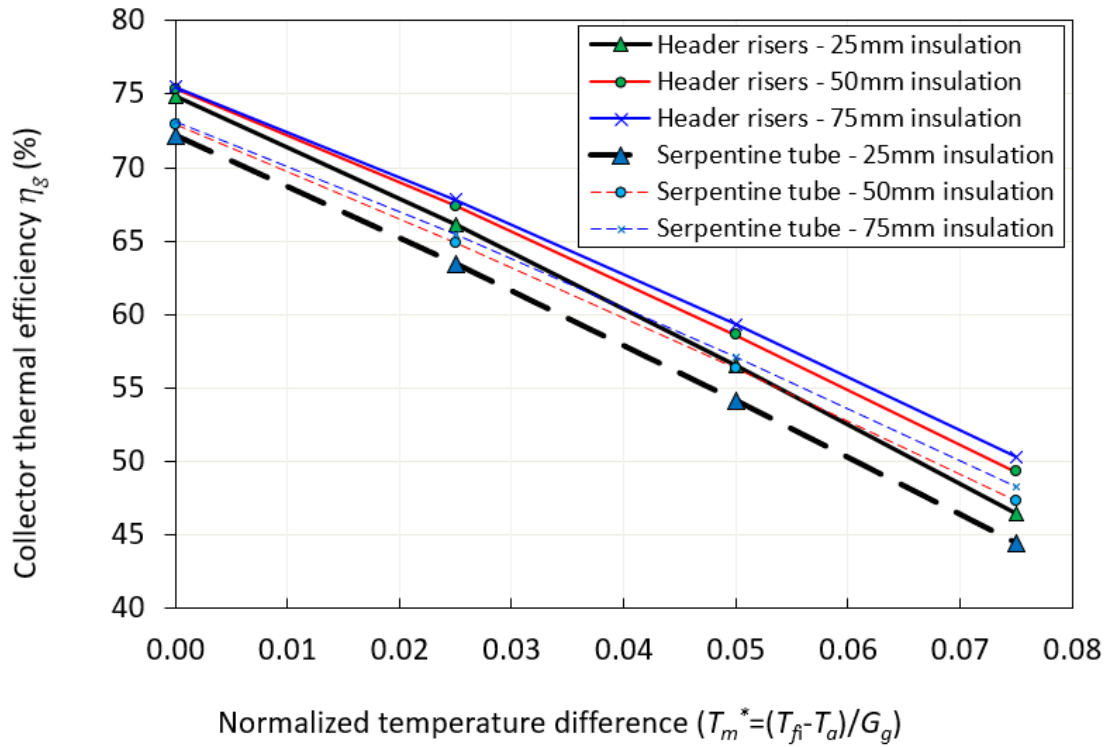
Figure 9 Thermal performance comparison of two configurations of FPSCs integrated with silicone tubing with different thermal insulation thicknesses at volume flow rate of 2.4 l/min

Table 3 Thermal performance parameters of two collector configurations integrated with silicone tubing with different thermal insulation at a volume flow rate of 2.4 l/min

| Type	Thermal insulation thickness (mm)	$\eta_0 = F_R(\tau\alpha)_{en}$	$F_R U_L$
Header risers	25	0.752	3.784
	50	0.757	3.474
	75	0.759	3.337
	100	0.760	3.311
Serpentine tube	25	0.724	3.703
	50	0.732	3.412
	75	0.734	3.320
	100	0.736	3.271

4.2 Test analysis on three different FPSC modules

4.2.1 Test results

According to the numerical predictions of the collector thermal performance, there is a small difference between two different configurations. Owing to limitations of experiment costs, just the configuration of the serpentine tube was selected for further experimental test. In view that the Chinese micro-channel heat pipe array flat plat collectors were proven to be having a good performance [15, 16], a Chinese micro-heat-pipe-array panel was ordered and modified with flexible silicone tubing for comparison. The aim was to explore thermal performance difference between flat plate collectors with common configurations (header risers, serpentine tube) and heat pipe flat plate collectors by integrating with freeze-tolerant silicone tubing. The original AES header riser panel (panel 1) without freeze-tolerant tube was also tested because it acted as a reference panel in accordance with one of the products of AES solar keymark. It helps to confirm the test accuracy with available collector thermal efficiency curve. As stated in section 3.2, totally, three solar panels were considered for tests.

Thermal performance tests of the three FPSC modules were executed on several clear days from 29th November to 3rd December 2017 at HWU Dubai campus. Figure 10 presents part of the measuring results on 30th November 2017. An average volume flow rate of 2.3 l/min was used in the test. In the conditions, the collector inlet temperature was close to the ambient temperature and the reduced temperature difference (T_m^*) was

close to zero, giving rise to a zero loss collector thermal efficiency.
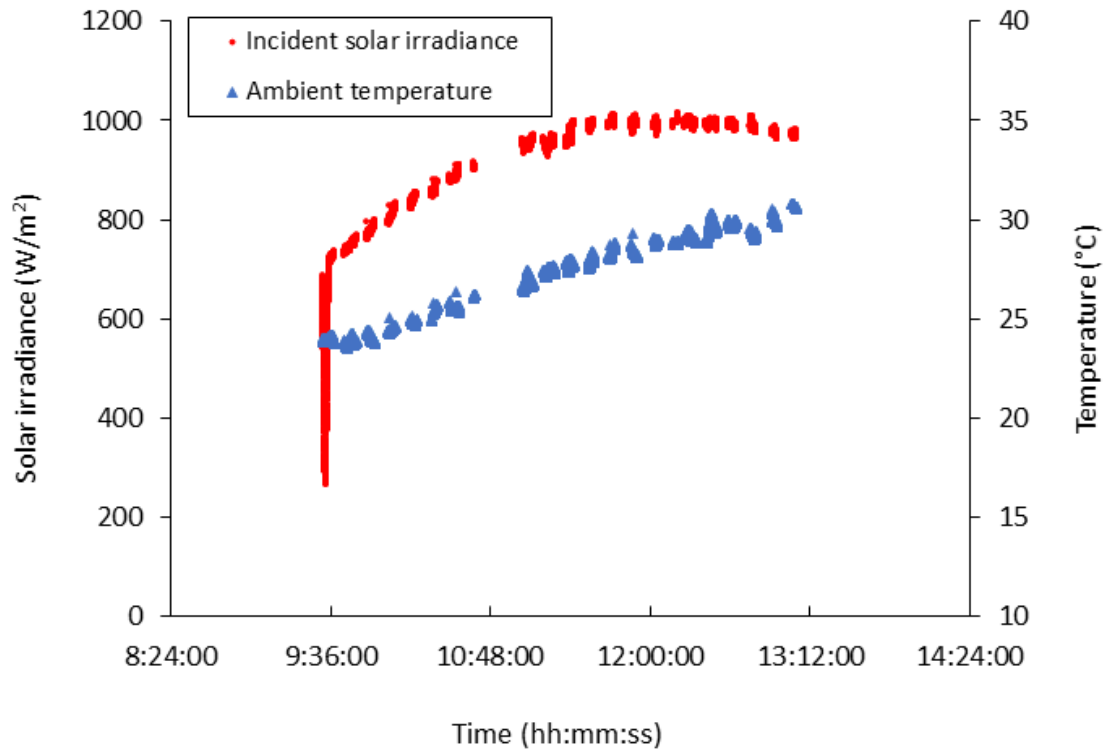
(a)
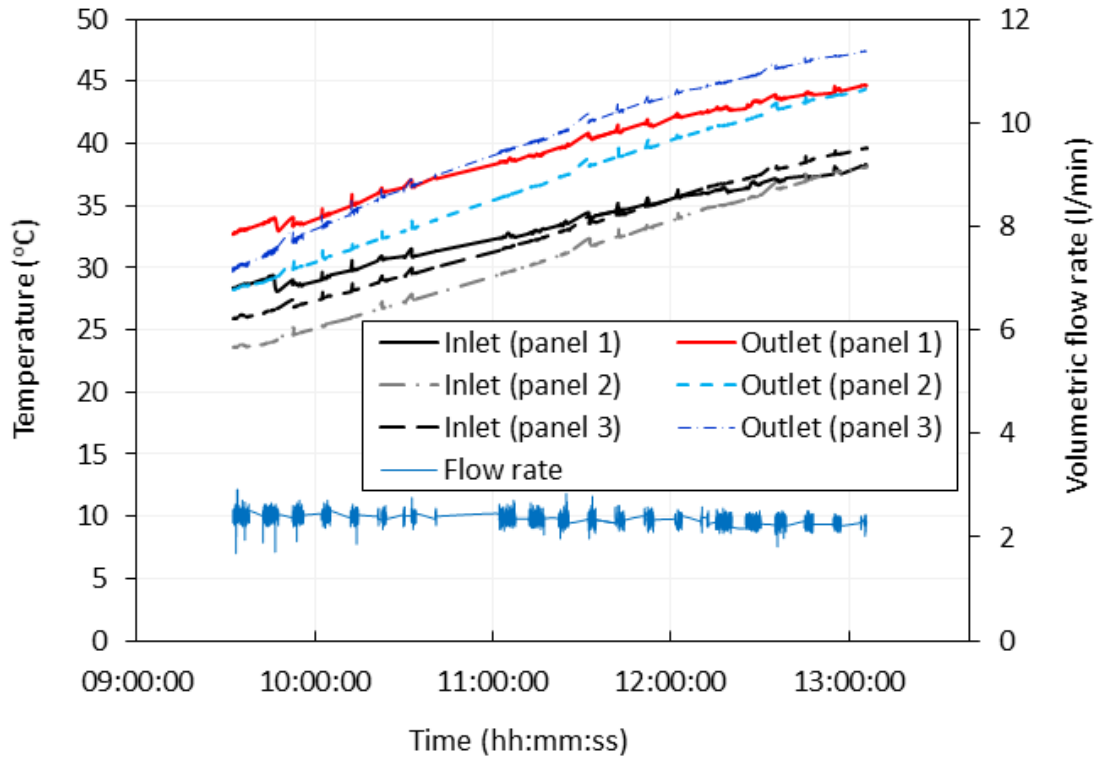
(b)

Figure 10 Measured variables of experimental tests for the three solar thermal panels

(a) measured meteorological conditions on 30 November 2017 in Dubai; (b) inlet and

outlet temperatures as well as flow rate

In determining the collector thermal performance, effective test data points of the

collector thermal efficiency should be obtained by selecting the data sampling with a

minimum incidence angle ($\pm 5°$) where the sun is normal to the collector tilted surface,

according to the test standard [51]. In this sense, it is necessary to take data samples

ideally close to solar noon time. The solar noon time in Dubai was referred to [52]. The

solar noon time of 29th November to 3rd December 2017 was during 12:06-12:08. It

can be seen from Figures 10(a) that the global solar irradiance on the collector surface

during the time slot of 11: 30 am–12:30 pm tends to be constant with a small fluctuation

($\pm$ 20 W/m^2), indicating that the test samples in the time slot can be used to calculate the collector thermal efficiency. Figure 11 gives the measured data points of the averaged collector thermal efficiencies under a flow rate of 2.3 l/min for the solar panels 1–3. It suggests that the collector zero loss efficiency of the three solar thermal collectors tends to be close to each other (around 68%).
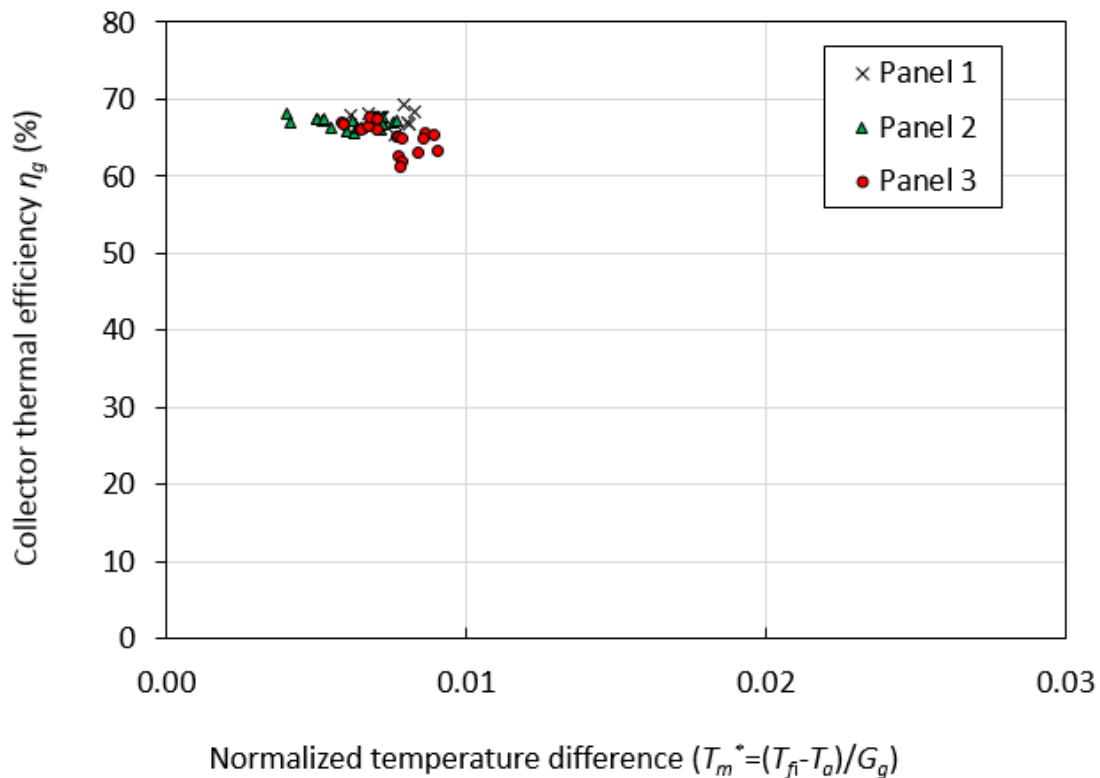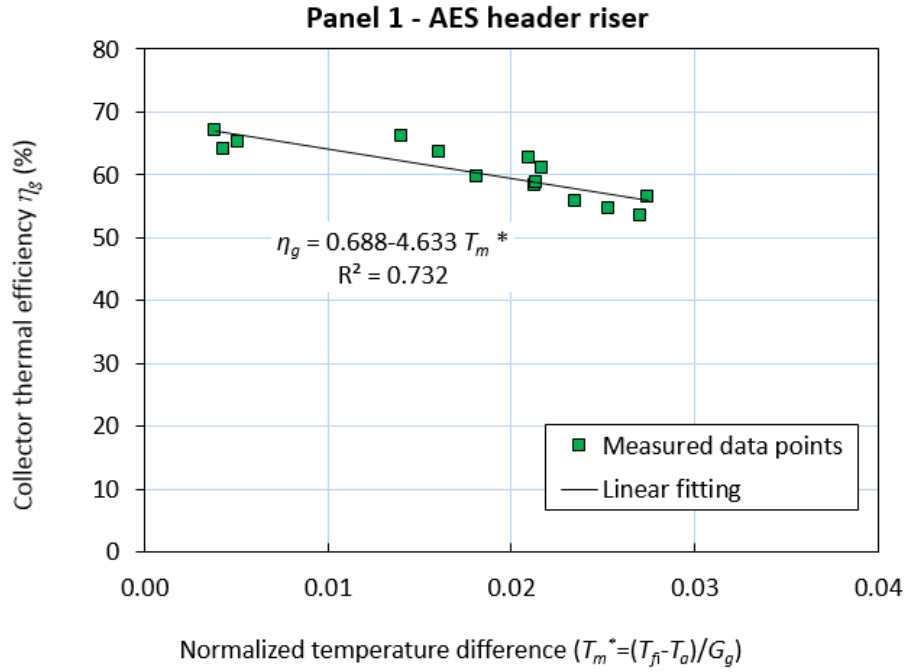

Figure 11 Measured data points close to the condition of zero loss collector efficiency under a flow rate of 2.3 l/min
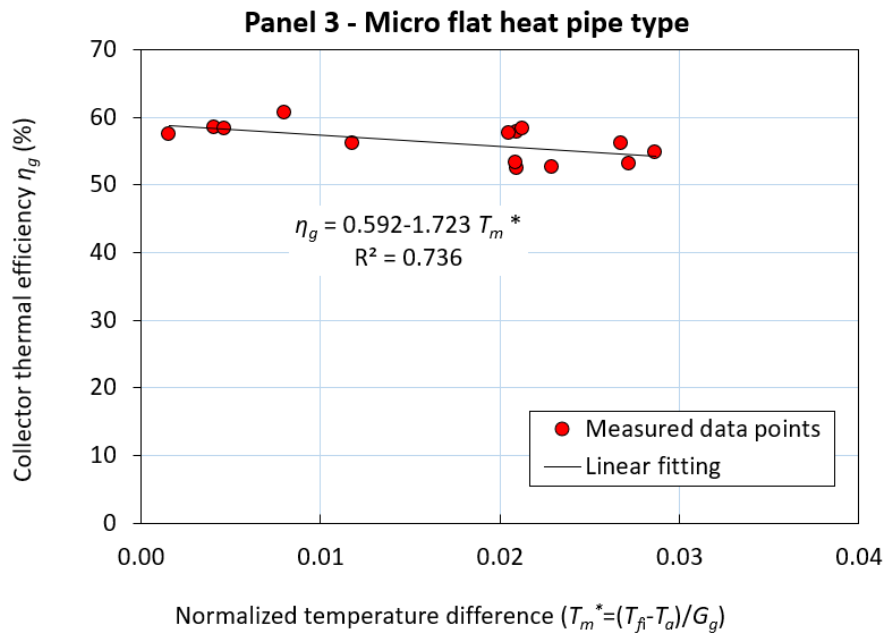
In order to get sufficient test data points of each solar panel for fitting collector thermal efficiency curves $\eta_g - T_m^*$ under a specific flowrate condition, extended tests on 3rd December 2017 with a flow rate of 1.7 l/min ($\pm$ 0.1 l/min) were executed with a higher collector inlet temperature to get larger reduced temperature differences. Figure 12

gives the thermal efficiency curves of solar panels 1 and 3, respectively, with a flow rate of 1.7 l/min (± 0.1 l/min), while the test result of the panel 2 has already been presented in Figure 8. The results indicate that AES header riser panel (panel 1) has the highest zero loss efficiency of 68.8%, but also the largest collector total heat loss coefficient of 4.633 W/(m^2 K). The AES serpentine tube panel (panel 2) performs in between. The collector total heat loss coefficient of the AES serpentine panel (panel 2) is reduced by 37.5% compared to that of the header riser reference panel, presumably due to the silicone tube inserted in the serpentine tube, which tends to act as a thermal insulation material with a low thermal conductivity. Although the panel 3 – the Chinese micro-heat-pipe-array panel has a relatively lower zero loss efficiency compared to the panels 1 and 2, it has the lowest heat loss coefficient 1.723 W/(m^2 K). It should be noted that the flow rate per m^2 collector aperture area of the panel 3 is somewhat lower than the other two panels, as a flow rate of 1.7 l/min has been used for all three panels but panel 3 has an aperture area of 1.853 m^2 different from the other two of 1.38 m^2. In this sense, a flow rate of 2.3 l/min should be used for the panel 3 for comparison (1.7 l/min/1.38 m^2×1.853 m^2 = 2.3 l/min). Referring to Figure 11, the zero loss efficiency of the panel 3 under the flow rate of 2.3 l/min is circa 0.68, which is close to that of the panel 1. From this point of view, the panel 3 performs slightly better than the other two panels as it has the lowest collector heat loss coefficient.

Panel 1 - AES header riser

$\eta_g = 0.688 - 4.633\ T_m^*$
$R^2 = 0.732$

Collector thermal efficiency η_g (%)

Normalized temperature difference $(T_m^* = (T_{fi} - T_a)/G_g)$

(a)

Panel 3 - Micro flat heat pipe type

$\eta_g = 0.592 - 1.723\ T_m^*$
$R^2 = 0.736$

Collector thermal efficiency η_g (%)

Normalized temperature difference $(T_m^* = (T_{fi} - T_a)/G_g)$

(b)

Figure 12 Thermal efficiency curve fittings of solar thermal panels under the flow rate

of 1.7 l/min (± 0.1 l/min) (a) the panel 1; (b) the panel 3

4.2.2 Comparison of three solar panels tested

It is necessary to examine the test results in comparison to the reference AES header

riser panel by the solar keymark certificate. The collector thermal efficiency curve of the solar keymark panel is provided in equation (22). Taking the solar keymark panel as a reference benchmark, measured data points and linear model fittings of the three solar panels 1–3 are compiled in Figure 13 for comparison. It indicates that the test result of the panel 1 agrees well with the reference solar keymark header riser panel, with relative errors of -5.1% and 0.2% for η_0 and U_L, respectively. The small deviation is presumably due to measuring uncertainties and different collector modules. Essentially, the panel 1 is the same type of solar panel as the solar keymark panel, with an identical size but not the same module. It confirms that the test results presented are credible and accurate. It is inferred that the panel 3 performs better than the solar keymark panel in terms of flow rate per m^2 collector aperture area, while the panel 2 performs somewhat lower than the solar keymark with $T_m^* \leq 0.035$ and better than the solar keymark when $T_m^* > 0.035$ (Typically, $T_m^* > 0.042$ for solar thermal systems working at a common temperature level of 50 °C with ambient temperature in the range of -5 –25 °C and average solar irradiance of 500-600 W/(m^2 K), resulting in a better performance of the panel 2 versus the solar keymark panel). Hence, the serpentine tube panel and the Chinese micro-heat-pipe-array panel integrated with silicone tubing for freeze tolerance are proven to be effective as the modification doesn't compromise the collector thermal performance remarkably.
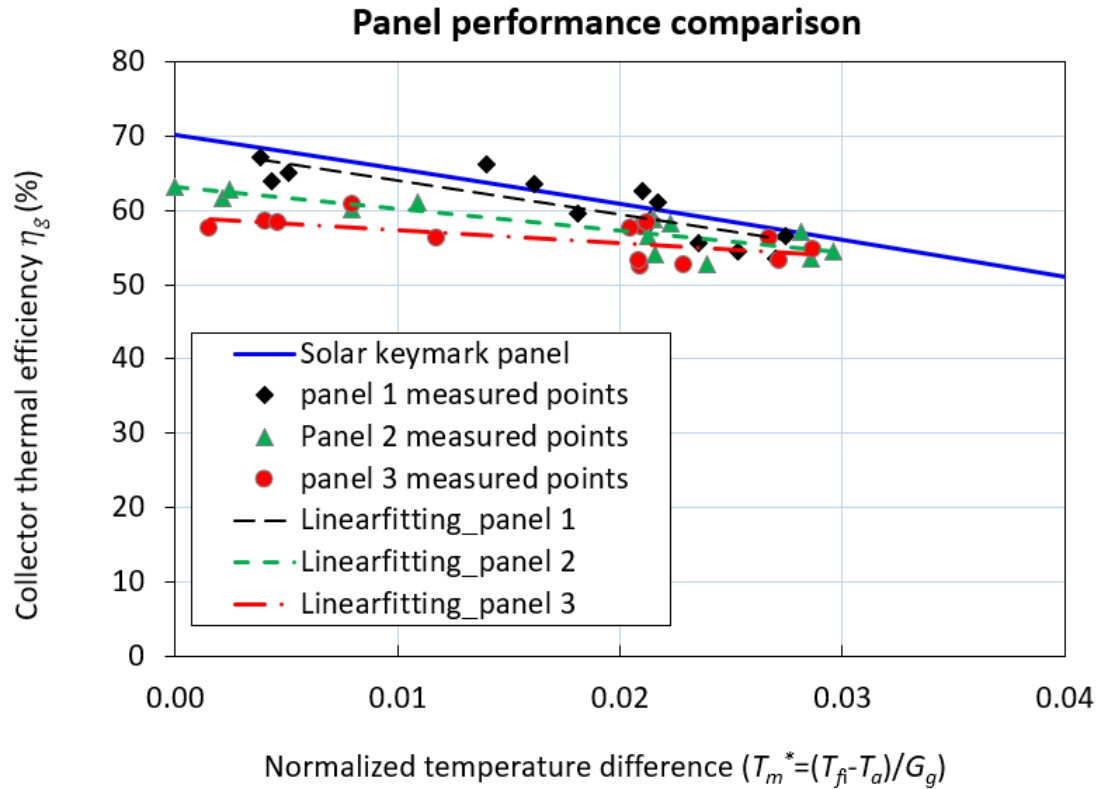
Figure 13 Thermal performance comparison of the three solar thermal collectors in contrast to the reference solar keymark panel under a flow rate of 1.7 l/min

5 Conclusions

A novel concept of flat plate solar collectors integrated with a freeze-tolerant solution is presented, and numerical calculations along with experimental tests are performed to analyze effective collector configurations.

(1) In the collector thermal performance predictions, the results show that the header riser panel integrated with silicone tubing performs slightly better than the serpentine tube panel. Zero loss collector thermal efficiencies of the serpentine tube panels are 3.4–3.9% lower than that of the header riser type, while the collector total heat loss coefficients (U_L) of the serpentine tube panels

are nearly the same as that of the header riser type. Increasing the thermal insulation thickness of PIR board above 50 mm has a minor impact on the collector thermal performance improvement for the studied solar panels.

(2) In further experimental tests of three representative solar panels (two of which were integrated with freeze-tolerant silicone tube), it is found that the original AES header-riser panel without silicone tubing has the highest zero loss efficiency of 68.8%, but also the largest collector heat loss coefficient of 4.633 W/(m^2 K) under a flow rate of 1.7 l/min. The Chinese micro-heat-pipe-array panel performs better than the AES header riser solar keymark panel in terms of flow rate per m^2 collector aperture area, while the AES serpentine tube panel with silicone tubing performs somewhat lower than the solar keymark with $T_m^* \leq 0.035$ and better than the solar keymark when $T_m^* > 0.035$.

(3) The collector total heat loss coefficient of the AES serpentine tube panel is reduced by 37.5% compared to that of the AES header riser panel, presumably due to the use of silicone tube in the serpentine tube. The serpentine tube panel and the Chinese micro-heat-pipe-array panel both integrated with silicone tubing for freeze tolerance are proven to be effective as the modification doesn't compromise the collector thermal performance markedly.

The information will be useful for real engineering, as it will enable a reduction of installed cost of conventional solar thermal systems with the freeze-tolerant solar thermal collectors developed, which directly run water, and there is no need to add secondary heat transfer facilities in the system.

Acknowledgment

References

[1] Sint NKC, Choudhury IA, Masjuki HH, Aoyama H. Theoretical analysis to determine the efficiency of a CuO-water nanofluid based-flat plate solar collector for domestic solar water heating system in Myanmar. Solar Energy 2017; 155: 608–619.

[2] Tian Z, Perers B, Furbo S, Fan J. Annual measured and simulated thermal performance analysis of a hybrid solar district heating plant with flat plate collectors and parabolic trough collectors in series. Applied Energy 2017; 205: 417–427.

[3] Li Q, Chen Q, Zhang X. Performance analysis of a rooftop wind solar hybrid heat pump system for buildings. Energy and Buildings 2013; 65: 75–83.

[4] Tian Z , Zhang S, Deng J, Fan J, et al., Large scale solar district heating plants in Danish smart thermal grid: Developments and recent trends, Energy Conversion

and Management 2019; 189:67–80.

[5] Kalogirou SA. Solar thermal collectors and applications. Progress in Energy Combustion Science 2004; 30: 231–295.

[6] Cerón, JF, Pérez-García J, Solano JP, García A, Herrero-Martín R. A coupled numerical model for tube-on-sheet flat-plate solar liquid collectors. Analysis and validation of the heat transfer mechanisms. Applied Energy 2015; 140: 275–287.

[7] Gunjo DG, Mahanta P, Robi PS. Exergy and energy analysis of a novel type solar collector under steady state condition: Experimental and CFD analysis. Renewable Energy 2017, 114: 655–669.

[8] Álvarez A, Tarrío-Saavedra J, Zaragoza S, López-Beceiro J, Artiaga R, Naya S, Álvarez B. Numerical and experimental study of a corrugated thermal collector. Case Studies in Thermal Engineering 2016; 8: 41–50.

[9] Del Col D, Padovan A, Bortolato M, Dai Prè M., Zambolin E. Thermal performance of flat plate solar collectors with sheet-and-tube and roll-bond absorbers. Energy 2013; 58: 258–269.

[10] Chen G, Doroshenko A, Koltun P, Shestopalov K. Comparative field experimental investigations of different flat plate solar collectors. Solar Energy 2015; 115:577–588.

[11] Facão J. Optimization of flow distribution in flat plate solar thermal collectors with riser and header arrangements. Solar Energy 2015; 120: 104–112.

[12] Fan J, Shah LJ, Furbo S. Flow distribution in a solar collector panel with horizontally inclined absorber strips. Solar Energy 2007; 81: 1501–1511.

[13] Zhou F, Ji J, Yuan W, Cai J, Tang W, Modjinoua M. Numerical study and experimental validation on the optimization of the large size solar collector. Applied Thermal Engineering 2018; 133: 8–20.

[14] Wang N, Zeng S, Zhou M, Wang S. Numerical study of flat plate solar collector with novel heat collecting components. International Communications in Heat and Mass Transfer 2015; 69: 18–22.

[15] Deng Y, Zhao Y, Wang W, et al. Experimental investigation of performance for the novel flat plate solar collector with micro-channel heat pipe array (MHPA-FPC). Applied Thermal Engineering 2013: 54(2): 440–449.

[16] Deng Y, Wang W, Zhao Y, Yao L, Wang X. Experimental study of the performance for a novel kind of MHPA-FPC solar water heater. Applied Energy 2013; 112: 719–726.

[17] Mansour MK. Thermal analysis of novel minichannel-based solar flat-plate collector. Energy 2013; 60: 333–343.

[18] Moss RW, Shire GSF, Henshall P, Eames PC, Arya F, Hyde T. Design and fabrication of a hydroformed absorber for an evacuated flat plate solar collector. Applied Thermal Engineering 2018; 138: 456–464.

[19] Saedodin S, Zamzamian SAH, Eshagh Nimvari M, Wongwises S, Javaniyan Jouybari H. Performance evaluation of a flat-plate solar collector filled with porous metal foam: Experimental and numerical analysis. Energy Conversion and Management 2017; 153: 278–287.

[20] Javaniyan Jouybari H, Saedodin S, Zamzamian A, Eshagh Nimvari M, Wongwises

S. Effects of porous material and nanoparticles on the thermal performance of a flat plate solar collector: An experimental study. Renewable Energy 2017, 114: 1407–1418.

[21] Tian Z, Perers B, Furbo S, Fan J. Thermo-economic optimization of a hybrid solar district heating plant with flat plate collectors and parabolic trough collectors in series. Energy Conversion and Management 2018; 165: 92–101.

[22] Furbo S, Dragsted J, Perers B, Andersen E, Bava F, Nielsen KP. Yearly thermal performances of solar heating plants in Denmark – Measured and calculated. Solar Energy 2018; 159: 186-196.

[23] Duffie JA, Beckman WA. Solar Engineering of Thermal Processes, 4th edition. John Wiley & Sons, New York, 2013.

[24] Deng J, Yang X, Ma R, Xu Y. Study on the thermodynamic characteristic matching property and limit design principle of general flat plate solar air collectors (FPSACs). Building Simulation 2016; 9(5): 529–540.

[25] Sarsam WS, Kazi SN, Badarudin A. A review of studies on using nanofluids in flat-plate solar collectors. Solar Energy 2015; 122: 1245–1265.

[26] Moghadam AJ, Farzane-Gord M, Sajadi M, Hoseyn-Zadeh M. Effects of CuO/water nanofluid on the efficiency of a flat-plate solar collector. Experimental Thermal and Fluid Science 2014; 58: 9–14.

[27] He Q, Zeng S, Wang S. Experimental investigation on the efficiency of flat-plate solar collectors with nanofluids. Applied Thermal Engineering 2015; 88: 165–171.

[28] Noghrehabadi A, Hajidavalloo E, Moravej M. Experimental investigation of

efficiency of square flat-plate solar collector using SiO2/water nanofluid. Case Studies in Thermal Engineering 2016; 8: 378–386.

[29] Verma SK, Tiwari AK, Chauhan DS. Performance augmentation in flat plate solar collector using MgO/water nanofluid. Energy Conversion and Management 2016; 124: 607–617.

[30] Sharafeldin MA, Gróf G, Mahian O. Experimental study on the performance of a flat-plate collector using WO_3/Water nanofluids. Energy 2017; 141: 2436–2444.

[31] Genc AM, Ezan MA, Turgut A. Thermal performance of a nanofluid-based flat plate solar collector: A transient numerical study. Applied Thermal Engineering 2018; 130: 395–407.

[32] Farajzadeh E, Movahed S, Hosseini R. Experimental and numerical investigations on the effect of Al_2O_3/TiO_2–H_2O nanofluids on thermal efficiency of the flat plate solar collector. Renewable Energy 2018; 118: 122–130.

[33] Verma SK, Tiwari AK, Tiwari S, Chauhan DS. Performance analysis of hybrid nanofluids in flat plate solar collector as an advanced working fluid. Solar Energy 2018; 167: 231–241.

[34] Verma SK, Tiwari AK, Chauhan DS. Experimental evaluation of flat plate solar collector using nanofluids. Energy Conversion and Management 2017; 134: 103–115.

[35] Helvaci HU, Khan ZA. Mathematical modelling and simulation of multiphase flow in a flat plate solar energy collector. Energy Conversion and Management 2015; 106:139–150.

[36] Shojaeizadeh E, Veysi F, Yousefi T, Davodi F. An experimental investigation on the efficiency of a Flat-plate solar collector with binary working fluid: A case study of propylene glycol (PG)–water. Experimental Thermal and Fluid Science 2014; 53: 218–226.

[37] Martin RH, Pérez-García J, García A, García-Soto FJ, López-Galiana E. Simulation of an enhanced flat-plate solar liquid collector with wire-coil insert devices. Solar Energy 2011; 85: 455-469.

[38] García A, Herrero-Martin R, Solano JP, Pérez-García J. The role of insert devices on enhancing heat transfer in a flat-plate solar water collector. Applied Thermal Engineering 2018; 132: 479-489.

[39] Zhou F, Ji J, Cai J, Yu B. Experimental and numerical study of the freezing process of flat-plate solar collector. Applied Thermal Engineering 2017; 118: 773–784.

[40] Liu H, Zhang S, Jiang Y, Yao Y. Feasibility study on a novel freeze protection strategy for solar heating systems in severely cold areas. Solar Energy 2015; 112: 144–153.

[41] Deng J, Tian Z, Fan J, et al. Simulation and optimization study on a solar space heating system combined with a low temperature ASHP for single family rural residential houses in Beijing. Energy and Buildings 2016; 126: 2–13.

[42] AES Solar Ltd., https://aessolar.co.uk/, accessed date: 12th June, 2019.

[43] Soltropy Ltd., https://www.soltropy.com/, accessed date: 12th June, 2019.

[44] Swinbank WC. Long-wave kinematic viscosity from clear skies. Quarterly Journal of the Royal Meteorological Society 1964; 90: 488–493.

[45] Kumar S, Mullick SC. Wind heat transfer coefficient in solar collectors in outdoor conditions. Solar Energy 2010; 84: 956–963.

[46] Hollands K, Unny TE, Raithby GD, Konicek L. Free convective heat transfer across inclined air layers. Journal of Heat Transfer - Transactions of the ASME 1976; 98(2): 189–193.

[47] SAS IP Inc., 2016. ANSYS FLUENT 18.0, USA.

[48] Versteeg HK and Malalasekera W. An Introduction to Computational Fluid Dynamics: The Finite Volume Method. Second Edition. Pearson Education Limited, London, UK, 2007.

[49] Fan J and Furbo S. Buoyancy driven flow in a hot water tank due to standby heat loss. Solar Energy 2012; 86: 3438–3449.

[50] ONG KS. Thermal performance of solar air heaters – mathematical model and solution procedure. Solar Energy 1995; 55: 93–109.

[51] The British Standards Institution. BS EN ISO 9806: 2013. Solar energy – Solar thermal collectors – Test methods. BSI Standards Limited, London, UK, 2013.

[52] https://www.timeanddate.com/astronomy/united-arab-emirates/dubai, accessed date: 3rd December, 2017.